Mon. Not. R. Astron. Soc. **389,** 1871–1880 (2008) doi:10.1111/j.1365-2966.2008.13697.x

The rate of Type Ia supernovae at $z \approx 0.2$ from SDSS-I overlapping fields

A. Horesh,[1⋆] D. Poznanski,[2] E. O. Ofek[3] and D. Maoz[1,4]

[1]*School of Physics and Astronomy and Wise Observatory, Tel Aviv University, Tel Aviv 69978, Israel*
[2]*Department of Astronomy, University of California, Berkeley, CA 94720-3411, USA*
[3]*Division of Physics, Mathematics and Astronomy, California Institute of Technology, Pasadena, CA 91125, USA*
[4]*Osservatorio Astrofisico di Arcetri, Largo Enrico Fermi 5, Firenze 50125, Italy*

Accepted 2008 July 8. Received 2008 July 8; in original form 2008 May 13

ABSTRACT

In the course of the Sloan Digital Sky Survey (SDSS-I), a large fraction of the surveyed area was observed more than once due to field tiling overlap, usually at different epochs. We utilize some of these data to perform a supernova (SN) survey at a mean redshift of $z = 0.2$. Our archival search, in ∼5 per cent of the SDSS-I overlap area, produces 29 SN candidates clearly associated with host galaxies. Using the Bayesian photometric classification algorithm of Poznanski et al., and correcting for classification bias, we find 17 of the 29 candidates are likely Type Ia SNe. Accounting for the detection efficiency of the survey and for host extinction, this implies a Type Ia SN rate of $r_{\rm Ia} = (14.0^{+2.5+1.4}_{-2.5-1.1} \pm 2.5) \times 10^{-14}\, h_{70}^2\, {\rm yr}^{-1}\, {\rm L}_{\odot,{\rm g}}^{-1}$, where the errors are Poisson error, systematic detection efficiency error and systematic classification error, respectively. The volumetric rate is $R_{\rm Ia} = (1.89^{+0.42+0.18}_{-0.34-0.15} \pm 0.42) \times 10^{-5}\, {\rm yr}^{-1}\, h_{70}^3\, {\rm Mpc}^{-3}$. Our measurement is consistent with other rate measurements at low redshift. An order of magnitude increase in the number of SNe is possible by analysing the full SDSS-I data base.

Key words: surveys – supernovae: general – cosmology: observations.

1 INTRODUCTION

Supernovae (SNe) play a central role in galaxy evolution and cosmic metal production. Measuring the rates at which SNe explode is thus an important step for understanding the chemical evolution of the Universe. In recent years, efforts have been intensified to measure the low-redshift Type Ia SN rate both in field environments (Cappellaro, Evans & Turatto 1999; Hardin et al. 2000; Madgwick et al. 2003; Blanc et al. 2004; Botticella et al. 2008; Dilday et al. 2008) and in galaxy clusters (Gal-Yam, Maoz & Sharon 2002; Maoz & Gal-Yam 2004; Sharon et al. 2007; Graham et al. 2008; Mannucci et al. 2008; Sand et al. 2008). However, due to small SN numbers, there are still significant uncertainties in low-redshift SN rates.

In this paper, we demonstrate that a large archival repository of SNe, one that is potentially useful for a low-redshift rate measurement using a large number of SNe, exists in the data from the first phase of the Sloan Digital Sky Survey (SDSS; York et al. 2000). We use a small fraction of these data to detect and compile a sample of SNe Ia and to derive the SN Ia rate at low redshift. The techniques we use in this paper are also of relevance for future projects such as the Panoramic Survey Telescope and Rapid Response System (Pan-STARRS; Kaiser 2004) and the Large Synoptic Survey Telescope (LSST; Tyson 2002). These projects will survey huge areas in a relatively short time, and will produce large samples of SNe for which spectral classification will not be possible, due to their large numbers.

In Section 2, we describe the SDSS data we use. The pipeline used to process these data and detect SNe is presented in Section 3. Detection efficiency and photometric calibration are discussed in Sections 4 and 5. Section 6 presents our preliminary results, including a first SN sample, its classification and a calculation of the SN Ia rate. We compare our results to previous measurements in Section 7, and summarize it in Section 8.

2 SDSS IMAGING DATA

The SDSS imaged about one quarter of the sky in five bands (u, g, r, i, z, centred at 3551, 4686, 6165, 7481, 8931 Å; Fukugita et al. 1996). Images were photometrically (Tucker et al. 2006) and astrometrically (Pier 2003) calibrated by the SDSS pipeline (Lupton et al. 2001). The data products of the SDSS (images and object catalogues) were made available[1] in a series of Data Releases (DR; see Adelman-McCarthy et al. 2008 for a description of the latest data release, DR6).

With the objective of covering the survey area once, imaging was performed by scanning the sky in great circles. Each scan was along a 2.°5-wide strip, where each strip was divided into numerous 'fields'. However, dividing the celestial sphere on to rectangular planes causes the rectangles to overlap, especially close to the poles

⋆E-mail: assafh@wise.tau.ac.il

[1] http://www.sdss.org

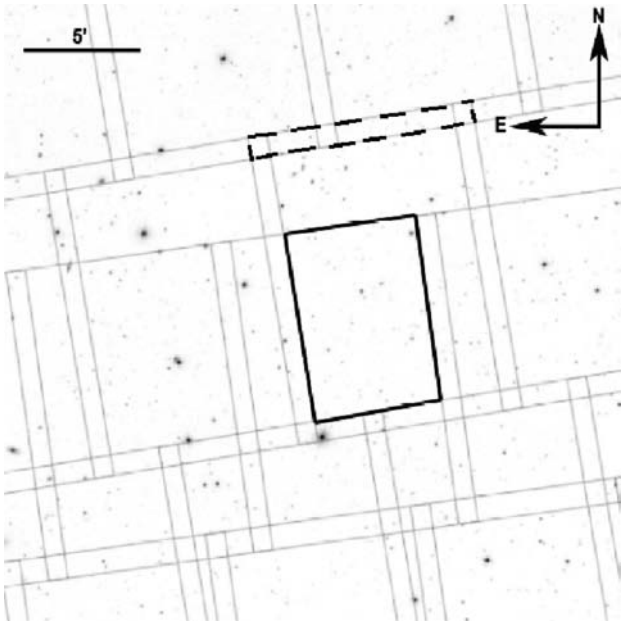

Figure 1. Examples of overlap between SDSS-I fields centred around RA = 14:56:49, Dec. = +10:57:48. The dashed polygon is an overlap between two adjacent strips which is used for SDSS quality checks, and the solid polygon is an overlap resulting from the mapping of the celestial sphere on to rectangles.

of the survey scan coordinate system (see e.g. Fig. 1). In addition, adjacent strips have an intentional overlap for the purpose of photometric and astrometric quality checks. The fact that different strips were imaged at different times raises the possibility of using the overlap regions to detect transient events.

Each final SDSS field is an image of 2048 × 1361 pixel. The image pixel scale is 0.396 arcsec with a median point spread function (PSF) of 1.4 arcsec in the *r* band. An exposure time of 53.9 s was used to image all fields, resulting in point source *AB* magnitude 95 per cent repeatability limits of 22.0, 22.2, 22.2, 21.3 and 20.5, in the *u*, *g*, *r*, *i*, *z* bands, respectively.

3 SUPERNOVA SURVEY DATA PIPELINE

To deal with the vast amount of data in the SDSS data base, we developed a largely automatic pipeline for downloading individual subsets of overlapping field images, and processing them one at a time. Our pipeline consists of three independent modules for download, registration and detection, executed in that order.

As a first step, we compiled a list of overlapping SDSS fields. To do so, we downloaded the coordinates of all the fields in the SDSS DR4 data base. By applying a polygon intersection algorithm, which assumes planar geometry, to the list of coordinates, we constructed a list of the overlapping regions of each SDSS field. Each image set, consisting of a first-epoch image (the 'reference' epoch) and its overlapping second epoch images, was individually downloaded for further processing by our pipeline. In the present paper, we search for SNe in the region $220^\circ < \mathrm{RA} < 240^\circ$, and $-1^\circ < \mathrm{Dec.} < 64^\circ$. This region is not far from the pole of the SDSS coordinate system ($\mathrm{RA} = 275^\circ$, $\mathrm{Dec.} = 0^\circ$), resulting in a large overlap area of 92 deg^2, obtained from 460 deg^2 of SDSS images.

Our survey search method is based on image subtraction. We note that an alternative method is to search for SNe in the SDSS catalogue using different criteria, e.g. SN colours (see Poznanski et al. 2002). However, a SDSS catalogue SN search has some disadvantages. For example, a blind colour search will be affected by colour contamination originating from SN host galaxies. In addition, lacking a direct access to the SDSS pipeline makes it difficult to estimate the survey detection efficiency function.

We chose to limit our SN search to the *g* and *r* bands since they are the deepest bands in the SDSS. Furthermore, the scanning order of each field in the SDSS is *r*, *i*, *u*, *z*, *g*. Therefore, the *r*- and *g*-band exposures of the same field in a given scan have the largest time separation, i.e. there is a ∼5 min difference between exposures of the same field in these bands. This time difference is critical for identifying and excluding Solar system objects from among the SN candidates.

Two computers were used for running our pipeline. One computer was used for continuous downloading of images from the SDSS data base. In parallel, the registration and detection modules (see below) were run on a computer with a Pentium IV 3.4 GHz processor and 2 GB of memory. The download rate and the processing rate both dictated a net data flow rate of about 1 deg^2 per day. In practice, software, hardware and communication problems resulted in a lower rate, and guided our decision to stop the current search after about 90 deg^2.

3.1 Image registration

The registration module aligns the overlapping images in each set to their reference image and produces a difference image in which SN candidates are searched for by the detection module. Both the *g* and *r* image sets, once downloaded, are registered separately by the registration module. An overlapping image is first registered to its reference image, based on their world coordinate system (WCS) coordinates, using the WREGISTER IRAF (Tody 1986) task. The overlapping areas are then cut out from both the reference and registered images. Using each field's photometric parameters, extracted from the SDSS data base,[2] we next linearly match the background level and the zero-point of the registered image to those of the reference image. At this point, we try to achieve a better image registration, which is crucial for image subtraction, by matching the positions of objects that appear in both images. We first detect objects in the overlapping image segments by applying the Source Extractor (SExtractor) program (Bertin & Arnouts 1996) to both segments. Next, by cross-correlating the object positions, a more precise registration between the two segments is obtained using the GEOMAP and GEOTRAN IRAF tasks, allowing for offsets in the *x*- and *y*-axes and a rotation angle between the two images. In order to avoid poor statistics in the matching process, this latter alignment is performed only if there are at least seven matching objects. Otherwise this stage is skipped.

Next, the image with the smaller PSF full width at half-maximum (FWHM) is degraded by convolving it with a 2D Gaussian kernel, $G(x, y) \propto \exp\,[-(x^2 + y^2)/2\sigma^2]$, in order to match the PSF of the second image. The kernel is found from the parameters of the two image PSFs, listed as 'psfWidth' in the SDSS catalogue 'Field' table. This simplistic PSF matching approach is dictated by the small number of objects (generally not point sources) in the overlapping regions, which prevents the application of more sophisticated PSF-matching algorithms (e.g. Alard & Lupton 1998; Alard 2000).

[2] http://casjobs.sdss.org/casjobs

Following subtraction of two registered images, the absolute values of the difference image is formed, so that all residuals are positive. In order to smooth out residuals due to imperfect alignment, the difference image is smoothed by convolving it with a 2D Gaussian, three pixels wide (1σ).

3.2 SN candidate detection

The residuals are detected in the difference image by applying SExtractor to the image. Since the final difference image is positive definite (see Section 3.1), it has a one-sided noise distribution. We chose to apply a 6σ detection threshold in the detection process. The value of the detection threshold is calculated using the Poisson fluctuations of the background counts in both the reference and registered images. The residuals detected by SExtractor are automatically examined in more detail to screen for various non-SN detection contaminations, as described next.

We first search for variable stars within our candidate list. Using SExtractor, we obtain a list of objects in both the registered and reference images. If an object is detected in both images at the same position where a residual was detected in the difference image, we query the SDSS catalogue for objects at that position. If an object, catalogued as a star, exists at that position, the candidate is considered a variable star and is rejected from our candidate list. Similarly, we reject candidates spectroscopically identified as quasars.

We next explore the possibility that a residual is the result of poor image registration. We search, using SExtractor, for positive residuals in two new difference images: the reference minus registered image and vice versa. If in each of the two images a residual is detected near the position of a candidate, we compare the difference between the photon counts of the two residuals to our detection threshold. In contrast to our original detection in the absolute value of the difference image, we now require the photon count difference to have at least 3σ significance. In a final test for improper alignment, a stamp of 41×41 pixels around the position of each residual is cut out of the registered and reference images. The two image stamps are re-registered using the xregister task in iraf, based on cross-correlation. A new difference image is produced using the new re-registered images. If no residuals are detected in the new subtracted stamp image, the candidate is discarded.

The remaining candidates are subjected to another test, aimed at determining whether or not they are moving objects. We first query the SDSS catalogue to check if the target has been flagged as a moving object. We also compare the position of each candidate in the *g* and *r* bands, assuming that it was detected in both bands. If the candidate position has changed by more than 2 pixels, it is also considered a moving object and is excluded from the candidate list. All stages up to this point are performed automatically, with no human intervention.

The remaining candidates are saved, together with their subtraction images, for visual inspection, performed by a single person (AH). The inspection helps reject false positives of various types, such as artefacts and residuals due to poor PSF matching, poor image alignment, cosmic rays and saturated objects (see Fig. 2). About 99 per cent of the candidates found by the automatic pipeline are discarded as false positives in the visual inspection stage.

4 DETECTION EFFICIENCY FUNCTIONS

Estimating the efficiency of our SN detection process is critical for deriving a reliable SN rate. We have planted a sample of fake SNe in the SDSS images, whose recovery fraction provides an estimate of the detection efficiency as a function of SN magnitude.

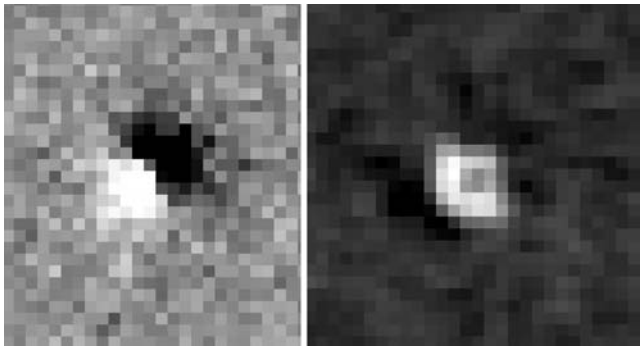

Figure 2. Examples of false positives which were rejected in the visual inspection stage. The left-hand panel shows a residual in the subtraction image due to image misalignment. The residual in the right-hand panel is due to poor PSF matching.

The first step in producing the fake SN sample was choosing the SN hosts. We compiled the *g* magnitude and the photometric redshift (Csabai et al. 2003; Oyaizu et al. 2008) of each galaxy in the overlapping sets of images from the SDSS catalogue. Under a simplifying assumption that the SN rate is proportional to stellar *g*-band luminosity, we selected a random subset of galaxies weighted by luminosity. To each of these selected hosts, we then assigned a fake SN. The SN was assigned a random *g*-band absolute magnitude in the range of -19.5 to -7.5. The absolute magnitudes were converted to observed magnitudes using a distance modulus based on the SN host photometric redshift (assuming a Hubble parameter of $H_0 = 70\,\mathrm{km\,s^{-1}\,Mpc^{-1}}$, a mass density in units of the critical density $\Omega_\mathrm{m} = 0.3$ and cosmological constant $\Omega_\Lambda = 0.7$). The SN *r*-band magnitude was randomly chosen to be in the range of -0.5 and $+1.5$ of the *g*-band magnitude, a range motivated by calculating synthetic *g* and *r* magnitudes from a set of observed spectra of SNe Ia (Nugent, Kim & Perlmutter 2002; Poznanski et al. 2002; Poznanski, Maoz & Gal-Yam 2007a).

The fake SNe were added to the real images as part of the data processing, prior to image registration, as follows. First, we randomly chose the image in which the SN was to be planted, i.e. either the reference image or the registered one. We then cut out a region around the fake SN host of size 1.5 times the host's 90 per cent light radius. SExtractor was applied to the host stamp image, producing a list of 10, 20, ... , 100 per cent light radii of the host. The radial distance of the fake SN from its host centre was chosen randomly from among these annuli, assuring that the locations of the artificial SNe roughly follow their galaxy host light. The final position of the fake SN with respect to the host was at a randomly chosen position angle. The SN was then planted in the selected image using the iraf task mkobjects.

The fake SN sample underwent the same processing as the real data, including the visual inspection stage, ensuring it faithfully reflected the actual detection efficiency. By spreading the fake SNe among all the overlapping fields, we also took into account the fact that the efficiency may vary from field to field.

Our detection efficiency functions in the *g* and *r* bands are shown in Fig. 3. We find that our efficiency level is $\sim$60 per cent, at best. This is probably due to the poor quality of image subtraction when the PSF matching and/or the registration are not perfect. For example, bright hosts often leave large residuals at their centres in the difference images. Therefore, a real SN that is close to its

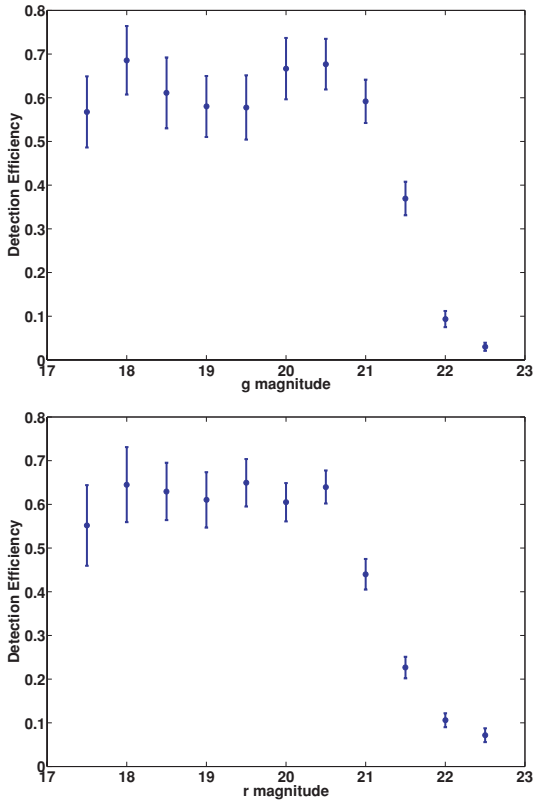

Figure 3. Detection efficiency functions in the g (top) and r (bottom) bands. Error bars represent 1σ Poisson errors.

host centre may be mistaken for an artificial residual due to poor registration, by either the pipeline or the human inspector. This effect seems to be independent of magnitude, even for bright SNe, due to the fact that such SNe will tend to be hosted by nearby, and hence bright, galaxies. It is also evident that the detection efficiency in the r band starts declining at brighter magnitudes, compared to the g band, probably due to the relative faintness of galaxies in the g band.

5 PHOTOMETRIC CALIBRATION

The SN candidates which pass the visual inspection are further explored. In order to obtain the magnitudes of these candidates, we download the images, in which a candidate resides, in the remaining (u, i, z) SDSS bands. Since the images of a field in different bands do not fully overlap, we first align them according to the image in which the candidate was detected (in either the g or the r band). We perform this alignment for the reference field images and for the registered field images separately. Then, the reference and registered field images in each band are processed by the same registration module used to originally process the g and r bands (see Section 3). After a final difference image is obtained in all five bands, 41×41 pixel images are cut out around the candidate.

These images are used to perform aperture photometry of the candidates. The counts are summed in an aperture of radius 2σ, where σ is 1/2.35 of the FWHM of the average PSF of a field (taken from the SDSS catalogue 'Field' table). With the zero-point, airmass and extinction parameters, also listed in the SDSS catalogue, we convert the candidate counts to magnitudes. To each magnitude we then apply an aperture correction that accounts for the flux outside the aperture. From aperture photometry on bright and isolated SDSS stars, we find mean aperture corrections of 0.21, 0.22, 0.23, 0.25, 0.25 in the u, g, r, i, z bands, respectively. With these corrections, our final magnitudes for bright stars also match those in the SDSS catalogue. We corrected the candidate magnitudes for Galactic extinction according to Schlegel, Finkbeiner & Davis (1998).

Table 1. Photometric errors.

Band	1σ Magnitude errors							
	19	19.5	20	20.5	21	21.5	22	22.5
u	0.10	0.11	0.17	0.16	0.17	0.26	0.36	0.45
g	0.10	0.13	0.13	0.12	0.17	0.17	0.24	0.24
r	0.11	0.11	0.17	0.13	0.15	0.32	0.30	0.29
i	0.11	0.14	0.16	0.22	0.24	0.63	0.55	0.50
z	0.18	0.19	0.26	0.60	0.62	0.69	0.86	0.61

To obtain realistic error estimates for our magnitude measurements, we have performed the same analysis on a large sample of artificial SNe. The artificial SNe were blindly planted in several images in the same manner as done for obtaining our detection efficiency functions (see Section 4). We expect the photometric errors to be larger than the usual Poisson errors due to inaccurate registration, varying backgrounds and residuals from the host galaxy subtraction. We planted ∼400 artificial SNe in each of eight magnitude bins (see Table 1). In each bin, and for each band, we calculate the root mean square (rms) of the difference between the measured magnitudes and the original magnitudes assigned to the artificial SNe, and adopt it as the systematic photometric error. The results are listed in Table 1.

6 RESULTS

6.1 SN sample

Our final candidate list for the 92 deg^2 of overlap area searched includes 47 transient candidates which we denote as SISN01 to 47, where SISN stands for SDSS-I SN. Among the candidates, 25 are clearly associated with a detected host galaxy, but offset from the nucleus (if there is one). Further 11 are, to within SDSS resolution, at the centres of their hosts. Final 11 candidates are 'hostless', i.e. cannot be unambiguously associated with any detected galaxy. Our criterion for hostlessness is being separated by both >5 arcsec and more than two times the 90 per cent light radius from any galaxy.

We first turn our attention to estimate the sample contamination by SN 'impostors'. Based on the SDSS limiting magnitudes (see Section 2), we estimate that a true SN Ia, at maximum light, will be undetectable at redshifts $z > 0.35$. Although there are exceptions, most core-collapse SNe are less luminous than SNe-Ia. Candidates with spectroscopic or photometric host redshifts with a 1σ lower limit above $z > 0.35$ are therefore excluded. Six of the seven candidates excluded by these criteria are at their host centres, and are thus likely to be active galactic nuclei (AGN), rather than SNe. The seventh candidate, SISN47, which is not at the centre of its host, might be a valid SN candidate falsely rejected due to an error in the photometric redshift of its host. However, if it were included in our final sample, it would have no effect on the total number of Type Ia SNe, being classified as a likely core-collapse SN (see Table 2).

The hostless candidates could either be real SNe which reside in galaxies below the SDSS limiting magnitude or can be

Table 2. SN candidate sample.

Id	RA	Dec.	β (deg)	u	g	r	i	z	$E(B-V)$	Redshift	P(Ia)	Sample
SISN01	15:44:10.57	+51:46:30.57	67.7	22.43	20.72	20.91	21.04	–	0.014	–	0.98	Hostless
SISN02	15:45:04.35	+40:11:38.27	57.7	20.94	20.95	21.54	21.80	21.65	0.016	0.13	0.02	Main
SISN03	14:56:43.00	+42:29:17.73	55.5	22.40	21.47	21.49	21.22	21.59	0.019	0.20	0.98	Main
SISN04	14:57:06.28	+46:37:25.51	59.0	21.61	21.31	21.64	21.07	22.38	0.015	0.61	0.42	High z
SISN05	14:56:48.96	+10:57:47.53	26.5	22.84	21.18	21.24	21.18	21.41	0.034	0.16	0.99	Main
SISN06	14:56:49.05	+36:36:56.41	50.3	22.05	20.36	20.56	20.74	21.65	0.015	0.20	1.00	Main
SISN07	14:42:59.88	+62:42:48.38	69.1	22.44	20.59	20.39	20.69	20.65	0.015	0.16	0.98	Main
SISN08	14:44:51.65	+06:55:48.55	21.8	20.36	20.39	20.50	20.71	21.25	0.033	0.76	0.01	High z
SISN09	14:46:19.33	+53:47:14.39	63.7	22.66	21.04	20.87	21.60	21.22	0.010	0.65	0.93	High z
SISN10	14:49:18.82	+52:33:07.73	63.0	23.66	21.54	21.35	21.66	21.23	0.015	**0.07**	0.02	Main
SISN11	15:00:35.10	+00:48:53.50	17.2	23.63	20.91	20.97	20.74	21.69	0.049	0.20	0.99	Main
SISN12	15:00:58.34	+29:04:11.96	43.8	22.57	20.98	20.50	20.89	21.25	0.018	0.04	0.19	Main
SISN13	15:02:35.07	+28:56:59.42	43.9	21.79	19.72	19.30	19.79	20.07	0.023	0.14	1.00	Main
SISN14	15:03:47.16	+04:56:04.76	21.3	–	21.96	20.97	21.19	20.82	0.040	0.44	0.39	Main
SISN15	15:07:33.29	+45:33:49.61	59.1	22.21	21.75	21.31	21.29	21.41	0.021	–	0.23	Hostless
SISN16	15:08:45.09	−00:38:53.27	16.3	23.41	21.07	20.51	20.33	21.06	0.065	–	0.74	Hostless
SISN17	15:08:37.26	+45:29:16.72	59.2	22.98	22.20	21.31	21.06	21.31	0.025	0.09	0.93	Main
SISN18	15:12:23.54	+02:40:28.03	19.8	22.44	21.18	21.15	21.01	–	0.041	0.23	1.00	Main
SISN19	15:12:44.37	+06:20:37.23	23.3	21.95	21.52	20.97	20.65	20.17	0.034	–	0.57	Hostless
SISN20	15:14:43.66	+04:39:55.11	21.9	–	21.31	21.12	20.91	20.81	0.051	0.10	0.19	Main
SISN21	15:16:38.95	+05:57:26.38	23.2	20.82	20.13	19.90	19.78	19.87	0.042	–	0.35	Hostless
SISN22	15:16:56.21	+47:10:04.82	61.4	21.10	21.47	20.86	21.22	22.26	0.030	0.94	0.00	High z
SISN23	15:17:32.35	+04:30:02.51	21.9	21.22	19.43	19.31	19.55	18.72	0.047	0.00	0.08	Main
SISN24	15:17:33.01	+39:19:52.54	54.6	22.24	20.81	20.71	21.09	21.36	0.017	–	0.95	Hostless
SISN25	15:22:29.67	+38:46:35.4	54.5	22.67	21.68	21.56	21.36	21.72	0.017	0.25	0.99	Main
SISN26	15:33:57.56	−00:48:42.1	17.9	21.50	20.27	20.25	20.48	21.16	0.116	**0.12**	1.00	Main
SISN27	15:33:07.47	+29:54:54.7	47.2	23.18	22.15	21.03	21.22	21.19	0.03	0.08	0.95	Main
SISN28	15:33:40.44	+09:16:37.1	27.6	20.62	20.57	20.72	20.59	20.96	0.041	0.05	0.02	Main
SISN29	15:37:37.48	−00:38:37.3	18.2	22.25	22.32	21.02	20.90	20.97	0.098	**0.16**	1.00	Main
SISN30	15:43:11.48	−00:23:55.6	18.8	21.70	20.70	20.38	20.14	19.96	0.096	0.04	0.04	Main
SISN31	15:45:27.58	+26:27:58.8	44.9	19.88	18.61	18.07	18.16	17.82	0.049	**0.03**	0.01	Main
SISN32	15:45:46.02	+35:37:06.7	53.4	21.73	20.02	19.55	19.98	20.59	0.029	0.06	0.97	Main
SISN33	15:46:03.12	+22:58:53.0	41.6	23.01	22.47	21.17	21.21	20.94	0.055	**0.12**	1.00	Main
SISN34	15:46:15.29	−00:37:05.8	18.8	21.76	19.83	19.25	18.91	18.94	0.103	–	0.06	Hostless
SISN35	15:46:48.36	+03:26:30.7	22.8	20.68	20.30	20.83	20.76	20.89	0.094	0.10	0.83	Main
SISN36	15:49:35.40	+39:59:10.9	57.8	22.28	21.17	20.49	20.15	20.55	0.012	0.56	0.86	Main
SISN37	15:51:22.86	+04:19:46.6	23.9	21.33	20.71	20.65	20.89	22.35	0.079	–	0.96	Hostless
SISN38	15:52:32.30	+25:38:47.8	44.6	22.58	20.58	20.02	20.35	21.72	0.060	–	0.99	Hostless
SISN39	15:52:55.62	+03:40:15.3	23.3	23.30	20.55	20.27	20.62	–	0.153	1.18	0.97	High z
SISN40	15:54:12.31	+24:15:30.8	43.3	23.52	21.85	21.11	21.24	22.42	0.048	0.08	0.59	Main
SISN41	15:54:52.01	+21:07:10.8	40.4	24.77	19.03	17.90	17.75	17.48	0.055	0.04	0.00	Main
SISN42	15:54:26.70	+03:41:09.8	23.4	21.85	20.00	19.65	19.57	19.69	0.154	–	0.64	Hostless
SISN43	15:55:53.55	+31:23:24.4	50.3	21.44	21.08	21.21	21.16	21.10	0.025	–	0.34	Hostless
SISN44	15:58:38.83	+05:15:48.3	25.2	22.12	19.95	19.22	19.84	20.05	0.056	**0.07**	1.00	Main
SISN45	15:59:11.36	+46:17:49.3	64.3	21.66	19.75	19.39	19.97	20.94	0.016	0.15	1.00	Main
SISN46	15:43:30.40	−01:11:51.3	18.1	21.64	21.00	21.52	21.85	21.05	0.117	0.56	0.79	High z
SISN47	15:39:04.47	+03:48:51.4	22.7	21.73	21.22	20.98	21.04	20.20	0.061	0.51	0.04	High z

Notes. Candidates with names in boldface are classified as Type Ia in the final sample. Magnitudes are before correction for Galactic extinction, derived from the reddening listed in the $E(B-V)$ column. Photometric errors are according to Table 1. Redshifts in boldface are spectroscopic. Candidates with no redshift are apparently hostless. The P(Ia) values of the candidates in the hostless and high-z samples were calculated assuming a uniform redshift probability distribution in the range $0 < z < 0.35$. β is the ecliptic latitude.

impostors such as quasars, slow-moving asteroids and variable stars. To estimate the expected fraction of SNe hosted by galaxies fainter than the SDSS limiting magnitude, we use the Blanton et al. (2003) galaxy luminosity function in the r band. The fraction of the stellar luminosity in galaxies with a luminosity $L < L_{\rm lim}$ is

$$P(L < L_{\rm lim}) = \frac{\int_0^{L_{\rm lim}} L\phi(L)\,{\rm d}L}{\int_0^{\infty} L\phi(L)\,{\rm d}L}, \quad (1)$$

where ϕ is the luminosity function. At $z = 0.2$, the mean redshift of SNe probed by our search (see Section 6.3), the SDSS r-band flux limit corresponds to an absolute magnitude of $M_r = -17.8$ mag and $P(L < L_{\rm lim}) = 23$ per cent. Again, assuming that SNe track the stellar luminosity, we therefore expect 23 per cent $\times$ 40 $\approx$ 9 candidates in galaxies below the SDSS limiting magnitude, consistent with the 11 hostless candidates we find. Conversely, this also argues that most of the hostless candidates are likely real SNe, as otherwise a large deficit of SNe in low-luminosity galaxies would be implied. None the less, due to the lack of redshifts for the hostless candidates, we are unable to determine with great confidence which of those candidates are real SNe and what are their types.

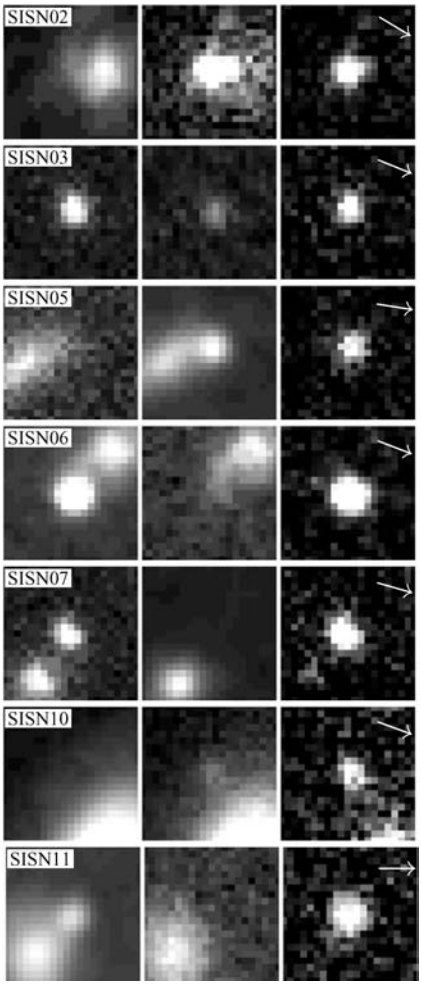

Figure 4. Final sample of SN candidates – for each candidate the reference (left-hand panel), registered (centre panel) and difference (right-hand panel) images are shown. Images are 16 arcsec on a side. Arrows indicate north, with east to the left when facing north.

We therefore exclude the 11 hostless candidates from our sample for the purpose of the SN rate calculation. The exclusion of the hostless candidates is accounted for in the luminosity-normalized SN rate calculation by using the luminosity density which originates from galaxies above the SDSS limiting magnitude (see Section 6.3).

Kuiper belt objects (KBOs) might also play a role as SN impostors. However, they are normally found near the ecliptic, while all our SN candidates have ecliptic latitude $\beta > 15^{\circ}$. Moreover, according to their magnitude distribution (Bernstein et al. 2004), their expected number in our survey, even near the ecliptic, is at least an order of magnitude lower than the observed number of SN candidates. We have checked for asteroids near the positions of all candidates in the Minor Planet Centre[3] and NASA Jet Propulsion Laboratory[4] data bases. No known asteroids were found within 5 arcmin of any candidates. Our final main SN sample thus consists of 29 candidates with hosts, among which five are nuclear and therefore may be AGNs. Figs 4–6 show sections of the reference, registered and difference images for each candidate in the final, hostless and high-z samples, respectively.

[3] http://www.cfa.harvard.edu/iau/mpc.html
[4] http://ssd.jpl.nasa.gov/sbfind.cgi

6.2 Supernova classification

Spectroscopic classification of our SN candidates is, of course, impossible in this archival survey. We therefore adopt a photometric classification method, the SN Automated Bayesian Classification (SN-ABC) routine of Poznanski et al. (2007a). This method compares the SN candidate magnitudes to a sample of SN spectral templates of different types, ages, redshifts and extinctions and returns the probability of a candidate being a Type Ia SN, P(Ia), as opposed to being a core-collapse SN. The routine uses as a prior the host redshift probability distribution function of each candidate. Six candidates in our sample have spectroscopic host redshifts. For the rest of the candidates, we retrieve photometric redshifts from the SDSS catalogue. We then assume Gaussian redshift probability distribution functions using the host spectroscopic or photometric redshifts and their errors.

We next perform an analysis similar to that of Poznanski et al. (2007b) in order to determine the degree of classification uncertainty and bias, i.e. what is the most probable real range in the fraction of SNe Ia, given the fraction that is classified as such. Using the SN spectral templates, we create a sample of fake SNe of the four most prevalent types: Ia, IIP, IIn and Ib/c. The distribution of redshifts is according to the redshift distribution of the galaxy sample used in the detection efficiency simulations (see Section 4). We note that while Types Ia and IIn are observable up to a redshift of $z \approx 0.35$, given the SDSS limiting magnitude, Types Ib/c and IIP are observable only out to $z \approx 0.15$. We find that, in our redshift range, the value of P(Ia) is not indicative of the actual probability of an object being a SN Ia. This is due to the fact that while SNe Ia usually are assigned very high values [85 per cent get $P(\mathrm{Ia}) > 0.9$] for core-collapse SNe, the results are less obvious. About half the Type IIn and Ib/c SNe and a fifth of the Type IIP SNe get misclassified, with values of $P(\mathrm{Ia}) > 0.5$. As a consequence, we use P(Ia) as a quality indicator, rather than a probability, cutting the sample at $P(\mathrm{Ia}) > 0.9$ where the contamination by core-collapse SNe is minimal. The fractions of simulated SNe that are classified or misclassified as Type Ia by the SN-ABC routine using the above threshold are 0.85, 0.04, 0.28 and 0.13 for Types Ia, IIP, IIn and Ib/c, respectively. Applying SN-ABC together with a $P(\mathrm{Ia}) > 0.9$ threshold on the 29 candidates in our sample results in 16 candidates which are classified as Ia, with χ^2 values in the range 0.3–10.6. Table 2 lists the candidate properties, including SN types and host redshifts.

Since we do not know the real fraction of Type Ia SNe at low redshift, we create a sample of possible fractions of different types, e.g. 30 per cent Ia, 50 per cent IIP, 10 per cent IIn, 10 per cent Ib/c, using steps of 10 per cent. For each set of fractions, we calculate the binomial probability of finding the observed 16 SNe Ia out of 29, using the fractions of SNe classified as Type Ia that we calculated for the four SN types. Each of the combinations is given a weight according to the number of permutations with the same fraction of SNe Ia. The outcome of this calculation is a probability distribution for the real number of SNe in our sample, given that 16 SNe were classified as Type Ia. From this probability function, we derive that the most probable 'true' number of SNe Ia in our sample is $N_{\mathrm{Ia}} = 17^{+3.8}_{-3.1} \pm 3.8$, where the first error is the 68 per cent range Poisson error, and the second one is a systematic 68 per cent range error due to the uncertainty in classification.

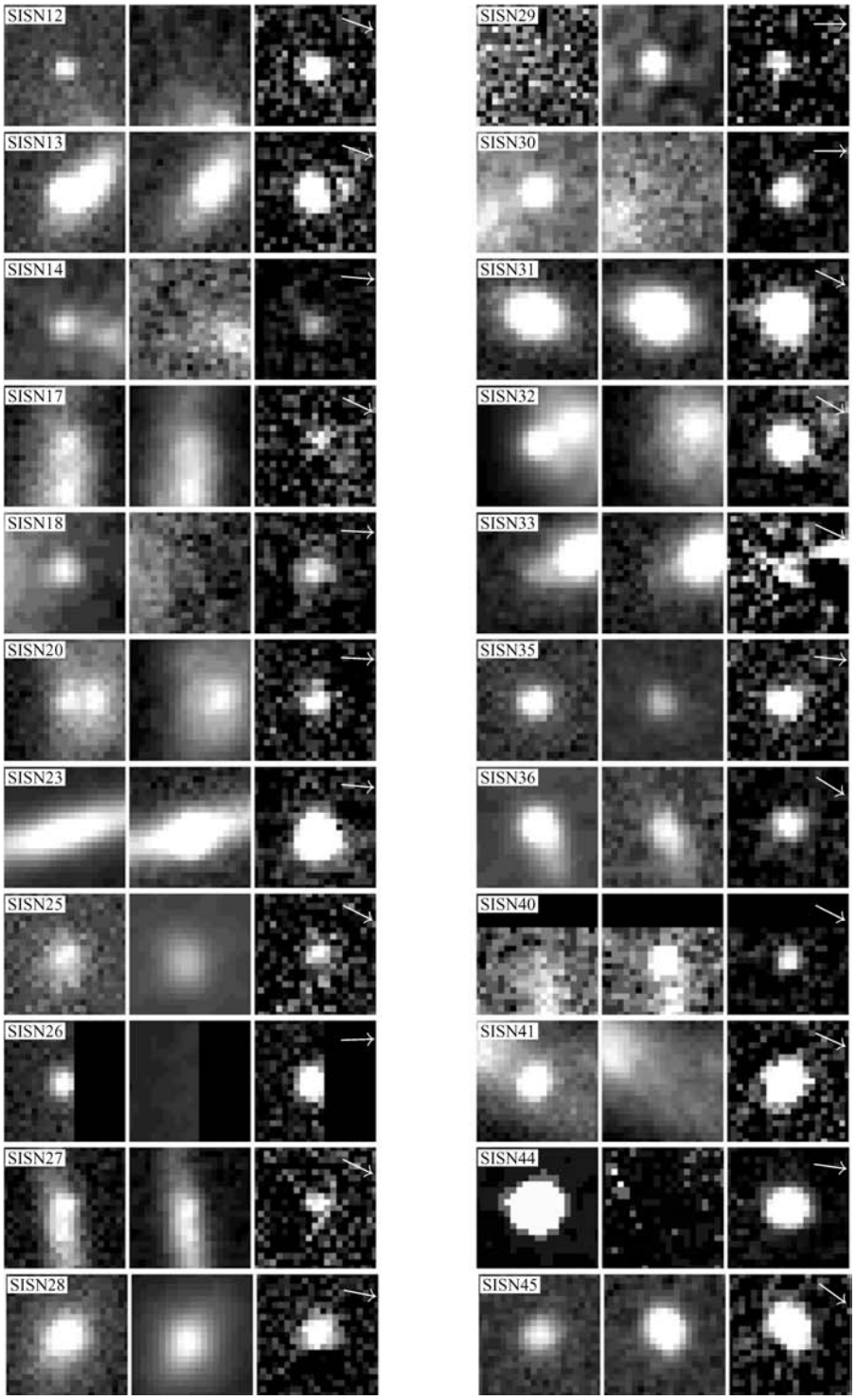

Figure 4 – *continued*

6.3 Supernova rate

We now derive the luminosity-normalized SN Ia rate, $r_{\rm Ia}$, in $\mathrm{SNu_{band}}$ units.[5] The rate is calculated using

$$r_{\rm Ia} = \frac{N_{\rm Ia}}{\sum_i \int \eta_i(z) j_{\rm lim}(z) \mathrm{d}V}, \quad (2)$$

where $N_{\rm Ia}$ is the number of SNe Ia, dV is a comoving volume element, $j_{\rm lim}$ is the luminosity density originating from galaxies which are above the SDSS limiting magnitude and $\eta_i(z)$ is the effective visibility time (or 'control time') of the ith image set, i.e. the time during which the SN is detectable. The integration is over the cosmological volume in each set, and the summation is over image sets. Given $\epsilon(m)$, the detection efficiency functions as a

[5] $1\ \mathrm{SNu_{band}} = \mathrm{SN}\ (100\,\mathrm{yr}\ 10^{10}\mathrm{L}_{\odot}^{\rm band})^{-1}$.

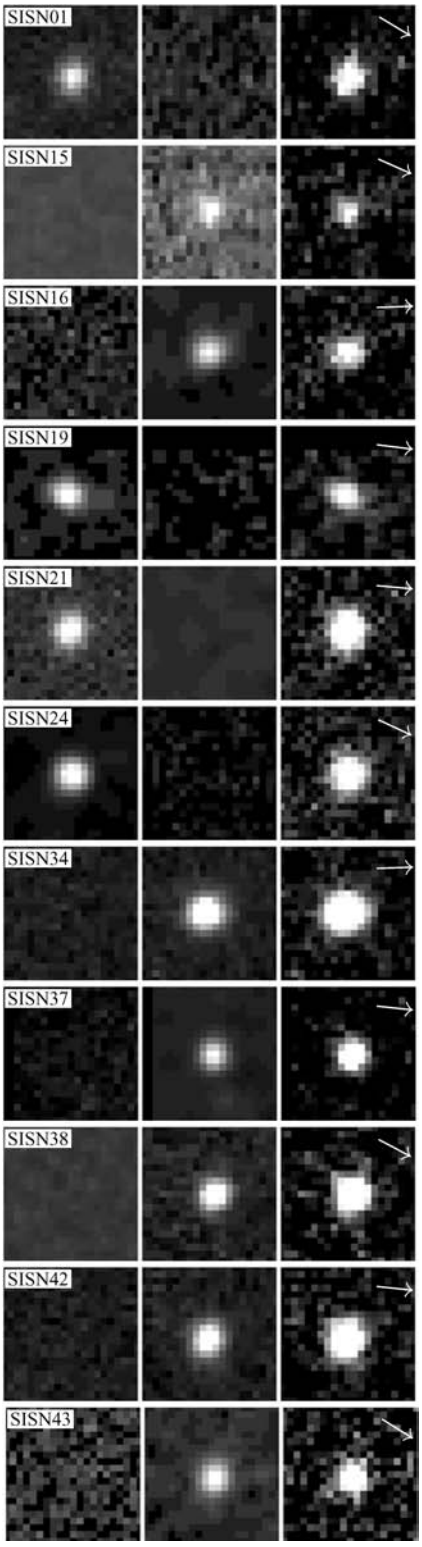

Figure 5. Same as Fig. 4 but for the hostless candidate sample.

function of magnitude m,

$$\eta_i(z) = \int \epsilon[m_{\rm eff}(t)] \frac{{\rm d}m_{\rm eff}}{{\rm d}t}\,{\rm d}t, \tag{3}$$

where $m_{\rm eff}(t)$ is the effective SN light curve determined by the time difference, Δt_i, between the reference and registered images in each

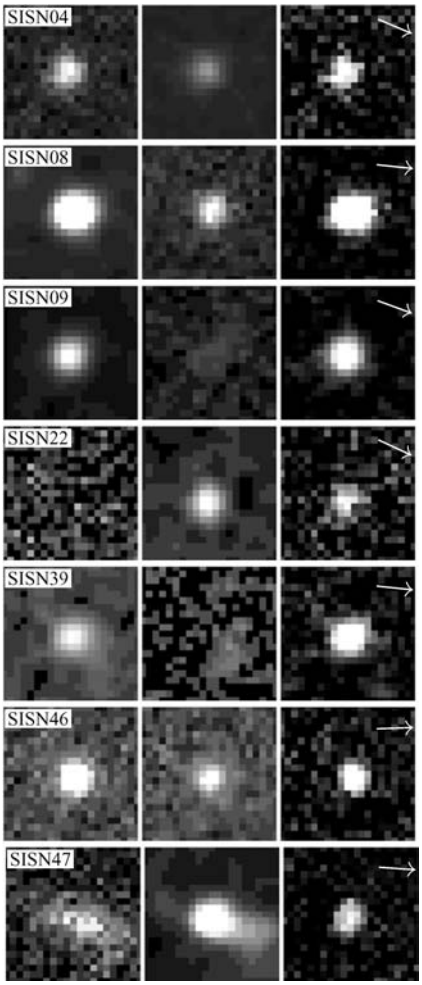

Figure 6. Same as Fig. 4 but for the high-z candidate sample, i.e. the seven candidates rejected based on their high photometric host redshifts.

set i,

$$m_{\rm eff}(t) = -2.5\log\left[10^{-0.4m(t)} - 10^{-0.4m(t+\Delta t_i)}\right]. \tag{4}$$

The mean redshift that we probe in this work, which depends on the visibility time and thus on the efficiency function, is given by

$$\langle z\rangle = \frac{\int \eta(z) z \,\frac{{\rm d}V}{{\rm d}z}\,{\rm d}z}{\int \eta(z)\frac{{\rm d}V}{{\rm d}z}\,{\rm d}z}. \tag{5}$$

In order to calculate the luminosity density, $j(z)$, we again use the Blanton et al. (2003) galaxy luminosity function. We convert their luminosity function, which is given for the SDSS bands shifted to $z = 0.1$, back to the rest-frame SDSS bands. We also account for luminosity evolution using their luminosity evolution parameter Q, thus obtaining the luminosity density as a function of redshift. Integrating over the luminosity function up to the limiting magnitude at each redshift provides $j_{\rm lim}(z)$.

The SN Ia rate must also be corrected for host extinction. Riello & Patat (2005) performed Monte Carlo simulations in which they modelled the dust distribution in host galaxies and accounted for various bulge-to-disc ratios and total optical depths. They found that the factor, f, by which SN Ia rates need to be corrected, is $1.27 < f < 1.91$, for Milky Way like dust. A similar, though lower, correction factor was derived by Neill et al. (2006), who derived the Type Ia SN rate at $z \approx 0.5$. Neill et al. (2006) considered

both Gaussian and exponential host extinction distributions in their detection efficiency simulations. They found a correction factor of $1.10 < f < 1.37$. Based on these studies, we adopt an intermediate correction factor of $f = 1.25$ to our SN rates.

The derived SN Ia rates in the g and r bands, using equation (2) and also correcting for host extinction, are

$$r^r_{\rm Ia} = \left(11.5^{+2.5+1.1}_{-2.5-0.9} \pm 2.5\right) \times 10^{-2}\, h^2_{70}\, {\rm SNu}_r,$$
$$r^g_{\rm Ia} = \left(14.0^{+2.5+1.4}_{-2.5-1.1} \pm 2.5\right) \times 10^{-2}\, h^2_{70}\, {\rm SNu}_g$$

at a mean redshift of $\langle z \rangle = 0.20$. The first error is due to the Poisson fluctuations in the SN number. The second is a systematic error due to the uncertainty in the detection efficiency function, calculated by using the efficiency function upper and lower (1σ) limits. The third error is the systematic classification error.

For comparison with previously published rates, we convert our luminosity-normalized rates also to a volumetric rate. We do so by replacing equation (2) with

$$R_{\rm Ia} = \frac{N_{\rm Ia}}{\sum_i \int \eta_i(z) \frac{j_{\rm lim}(z)}{j_{\rm total}(z)}\, {\rm d}V}, \quad (6)$$

where $j_{\rm total}$ is the total luminosity density. The resultant volumetric rates are then

$$R^r_{\rm Ia}(0.2) = \left(1.75^{+0.40+0.17}_{-0.32-0.14} \pm 0.40\right) \times 10^{-5}\ {\rm yr}^{-1}\, h^3_{70}\, {\rm Mpc}^{-3},$$
$$R^g_{\rm Ia}(0.2) = \left(1.89^{+0.42+0.18}_{-0.34-0.15} \pm 0.42\right) \times 10^{-5}\ {\rm yr}^{-1}\, h^3_{70}\, {\rm Mpc}^{-3}.$$

The difference between these two volumetric rates is due to the different evolution of the luminosity density in each band. This difference is an inherent weakness of deriving volumetric rates from luminosity-normalized rates, but in our case the difference is smaller than any of the other sources of uncertainty.

7 COMPARISON WITH PREVIOUS MEASUREMENTS

In this section, we compare our rate measurements to previously reported low-redshift SN rates. Most of these measurements (e.g. Cappellaro et al. 1999; Hardin et al. 2000; Blanc et al. 2004) were given in B-band SNu units. These rates were then converted to volumetric rates using the luminosity density at the relevant redshift. However, various luminosity functions were used to convert to volumetric rates. For example, Blanc et al. converted their rate and the rates of Cappellaro et al. (1999), Hardin et al. (2000) and Madgwick et al. (2003) using the 2dF redshift survey luminosity density (Cross et al. 2001). In contrast, Botticella et al. (2008) fit a set of luminosity density measurements (Norberg et al. 2002; Blanton et al. 2003; Bell et al. 2004; Faber et al. 2007; Tresse et al. 2007) with a smooth function of redshift, and used it to perform the conversion to volumetric rates. We will repeat the Botticella et al. (2008) conversion of volumetric rates of previously published luminosity-normalized rates (see Table 3), using their redshift-dependent luminosity density,

$$j_B(z) = (1.03 + 1.76 \times z) \times 10^8\ {\rm L}^B_\odot\ {\rm Mpc}^{-3}. \quad (7)$$

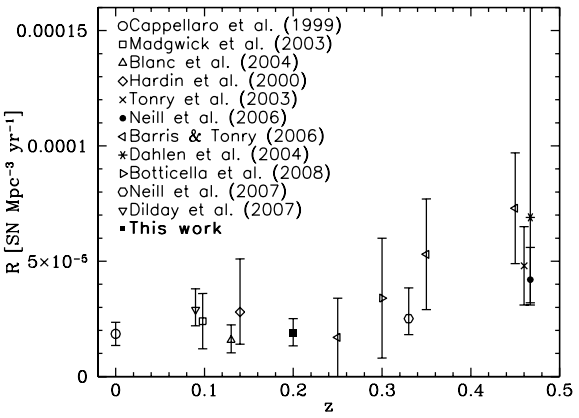

Figure 7. Type Ia SN rates from different authors (see legend). Error bars are from quadrature additions of the various errors listed in Table 3.

Dilday et al. (2008) have recently reported a Type Ia SN rate from the SDSS-II Supernova Survey (Frieman et al. 2008). The majority of SNe found in this survey, in contrast to our survey, have been confirmed spectroscopically (resulting in a lower redshift range being probed). The SN Ia rate measured by Dilday et al., based on 17 SNe at $z \sim 0.09$, is higher than our rate measurement by a factor of $\sim$1.5 but consistent within the errors. Table 3 shows these various low-redshift rate measurements and Fig. 7 shows a compilation of rate measurements to $z < 0.5$.

Our rate measurement is consistent with other low-redshift rate measurements, and ranks with the most accurate among them. However, as mentioned above, some of the previously published volumetric rates, which appear in Table 3, would change, depending on the luminosity density that is used to derive them. A remaining uncertainty in such comparison arises from the fact that the rates in SNu of Cappellaro et al. (1999), Madgwick et al. (2003), Blanc et al. (2004) and Hardin et al. (2000) are multiplied by the luminosity density at the *mean* redshift of each survey, thus not taking

Table 3. Comparison of low-redshift Type Ia SN rate measurements.

$\langle z \rangle$	$N_{\rm Ia}$	$R_{\rm Ia}$			Author
		h^2_{70} SNu $_B$	h^2_{70} SNu $_g$	$10^{-5}\,{\rm yr}^{-1}\, h^3_{70}\, {\rm Mpc}^{-3}$	
$\sim$0	70	0.18 ± 0.05		1.85 ± 0.5	Cappellaro et al. (1999)[b]
0.09	17		$0.235^{+0.07}_{-0.06}$	$2.9^{+0.9}_{-0.7}$	Dilday et al. (2008)[a]
0.098	19	0.196 ± 0.098		2.4 ± 1.2	Madgwick et al. (2003)[b]
0.13	14	$0.125^{+0.044+0.028}_{-0.034-0.028}$		$1.58^{+0.56+0.35}_{-0.43-0.35}$	Blanc et al. (2004)[b]
0.14	4	$0.22^{+0.17+0.06}_{-0.10-0.03}$		$2.8^{+2.2+0.7}_{-1.3-0.4}$	Hardin et al. (2000)[b]
0.2	**17**	$\mathbf{0.14^{+0.03+0.01}_{-0.03-0.01} \pm 0.03}$	$\mathbf{0.14^{+0.03+0.01}_{-0.03-0.01} \pm 0.03}$	$\mathbf{1.89^{+0.42+0.18}_{-0.34-0.15} \pm 0.42}$	**This work**
0.25	1			1.7 ± 1.7	Barris & Tonry (2006)

[a]Luminosity-normalized rate derived from a volumetric rate.
[b]These rates have been converted to volumetric rates using the redshift-dependent luminosity density function from Botticella et al. (2008).

into account that the effective volume of the survey is a function of redshift.

In order to compare our luminosity-normalized rate in SNu_g units also to rates given in SNu_B units, we adopt the Lupton (2005) conversion between B- and g-band magnitudes,

$$B = g + 0.2271 + 0.313(g - r). \quad (8)$$

Using the mean luminosity-weighted colour, $g - r = 0.53$, of the SDSS galaxy subset sample described in Section 4, together with equation (8), implies a factor of 1.03 increase going from SNu_g units to SNu_B units. Using this factor, our rate measurement in SNu_B units is $r_{\rm Ia} = (14.4^{+2.6+1.4}_{-2.6-1.1} \pm 2.6) \times 10^{-2}\, h_{70}^2\, SNu_B$. As seen in Table 3, this again agrees with previous measurements.

8 SUMMARY

We have conducted a low-redshift photometric SN survey using archival data from SDSS-I overlapping fields. Based on the number of Type Ia SNe that we find, $N_{\rm Ia} = 17^{+3.8}_{-3.1} \pm 3.8$, and keeping track of the various sources of error and bias, we have derived a SN Ia rate of $r^g{}_{\rm Ia} = (14.0^{+2.5+1.4}_{-2.5-1.1} \pm 2.5) \times 10^{-2}\, h_{70}^2\, SNu_g$, or a volumetric rate of $R^g{}_{\rm Ia} = (1.89^{+0.42+0.18}_{-0.34-0.15} \pm 0.42) \times 10^{-5}\, {\rm yr}^{-1}\, h_{70}^3\, {\rm Mpc}^{-3}$. Our derived rates are consistent with previous measurements, but rank with the most accurate ones. However, SN Ia rates at low redshift, including ours, still suffer from several sources of uncertainty. In our case, the uncertainty is mostly due to small numbers. The derivation of volumetric rates using different luminosity functions and different extinction corrections is another source of ambiguity when comparing different measurements at similar redshifts, and when comparing observations with model predictions. Nevertheless, we have shown that there is a vast amount of archival SDSS data that can be used for studying SNe at a low cost. The full SDSS-I SN sample, once mined, would include several hundreds of SNe, comparable to the ∼500 expected from SDSS-II (a survey designed specifically for finding SNe). Assuming a similar fraction of Type Ia SNe as we found, both the Poisson and binomial classification uncertainties for such a large sample would be reduced to the ∼5 per cent level, while the uncertainty due to the detection efficiency function will remain the same. Although SNe found by archival search methods, such as ours, cannot be studied spectroscopically, a full SDSS-I sample could be useful for improved investigations of SN rates as a function of galaxy type and environment.

ACKNOWLEDGMENTS

Funding for the SDSS and SDSS-II has been provided by the Alfred P. Sloan Foundation, the Participating Institutions, the National Science Foundation, the US Department of Energy, the National Aeronautics and Space Administration, the Japanese Monbukagakusho, the Max-Planck Society and the Higher Education Funding Council for England. The SDSS web site is http://www.sdss.org/. We thank the anonymous referee for comments that improved the presentation.

REFERENCES

Adelman-McCarthy J. K. et al., 2008, ApJS, 175, 297
Alard C., 2000, A&AS, 144, 363
Alard C., Lupton R. H., 1998, ApJ, 503, 325
Barris B. J., Tonry J. L., 2006, ApJ, 637, 427
Bell E. F. et al., 2004, ApJ, 600, L11
Bernstein G. M., Trilling D. E., Allen R. L., Brown M. E., Holman M., Malhotra R., 2004, AJ, 128, 1364
Bertin E., Arnouts S., 1996, A&AS, 117, 393
Blanc G. et al., 2004, A&A, 423, 881
Blanton M. R. et al., 2003, ApJ, 592, 819
Botticella M. T. et al., 2008, A&A, 479, 49
Cappellaro E., Evans R., Turatto M., 1999, A&A, 351, 459
Cross N. et al., 2001, MNRAS, 324, 825
Csabai I. et al., 2003, AJ, 125, 580
Dahlen T. et al., 2004, ApJ, 613, 189
Dilday B. et al., 2008, ApJ, 682, 262
Faber S. M. et al., 2007, ApJ, 665, 265
Frieman J. A. et al., 2008, AJ, 135, 338
Fukugita M., Ichikawa T., Gunn J. E., Doi M., Shimasaku K., Schneider D. P., 1996, AJ, 111, 1748
Gal-Yam A., Maoz D., Sharon K., 2002, MNRAS, 332, 37
Graham M. L. et al., 2008, AJ, 135, 1343
Hardin D. et al., 2000, A&A, 362, 419
Kaiser N., 2004, SPIE, 5489, 11
Madgwick D. S., Hewett P. C., Mortlock D. J., Wang L., 2003, ApJ, 599, L33
Mannucci F., Maoz D., Sharon K., Botticella M. T., Della Valle M., Gal-Yam A., Panagia N., 2008, MNRAS, 383, 1121
Maoz D., Gal-Yam A., 2004, MNRAS, 347, 951
Neill J. D. et al., 2006, AJ, 132, 1126
Neill J. D. et al., 2007, in Di Salvo T. et al., eds, Proc. AIP Conf. Ser. Vol. 924, The Multicolored Landscape of Compact Objects and their Explosive Origins: Cefalu 2006. Am. Inst. Phys., New York, p. 421
Norberg P. et al., 2002, MNRAS, 336, 907
Nugent P., Kim A., Perlmutter S., 2002, PASP, 114, 803
Lupton R. H., 2005, AJ, submitted
Lupton R., Gunn J. E., Ivezić Z., Knapp G. R., Kent S., 2001, in Harnden F. R., Jr, Primini F., Payne H. E., eds, ASP Conf. Ser. Vol. 238, Astronomical Data Analysis Software and Systems X. Astron. Soc. Pac., San Francisco, p. 269
Oyaizu H., Lima M., Cunha C. E., Lin H., Frieman J., Sheldon E. S., 2008, ApJ, 674, 768
Pier J. R., Munn J. A., Hindsley R. B., Hennessy G. S., Kent S. M., Lupton R. H., Ivezić Ž., 2003, AJ, 125, 1559
Poznanski D., Gal-Yam A., Maoz D., Filippenko A. V., Leonard D. C., Matheson T., 2002, PASP, 114, 833
Poznanski D., Maoz D., Gal-Yam A., 2007a, AJ, 134, 1285
Poznanski D. et al., 2007b, MNRAS, 382, 1169
Riello M., Patat F., 2005, MNRAS, 362, 671
Sand D. J., Zaritsky D., Herbert-Fort S., Sivanandam S., Clowe D., 2008, AJ, 135, 1917
Scannapieco E., Bildsten L., 2005, ApJ, 629, L85
Schlegel D. J., Finkbeiner D. P., Davis M., 1998, ApJ, 500, 525
Sharon K., Gal-Yam A., Maoz D., Filippenko A. V., Guhathakurta P., 2007, ApJ, 660, 1165
Tody D., 1986, SPIE, 627, 733
Tonry J. L. et al., 2003, ApJ, 594, 1
Tresse L. et al., 2007, A&A, 472, 403
Tucker D. L. et al., 2006, Astron. Nachr., 327, 821
Tyson J. A., 2002, SPIE, 4836, 10
York D. G. et al., 2000, AJ, 120, 1579

This paper has been typeset from a TEX/LATEX file prepared by the author.